RSC Advances

PAPER

View Article Online
View Journal | View Issue

Cite this: *RSC Adv.*, 2025, **15**, 8541

Construction of $CeCu_x$-BTC/CN S-type heterojunctions and photocatalytic CO_2 reduction to CO and CH_4

Hui Zhang,[abc] Yi Hui Sun,[abc] Sheng Li An,[abc] Rui Hua Guo,[abc] Rui Fen Wang*[abc] and Yu Wei Ma[abc]

S-type heterojunction photocatalysts ($CeCu_x$-BTC/CN) of cerium-copper bimetallic organic framework ($CeCu_x$-BTC) and graphitic carbon nitride (g-C_3N_4) were constructed by a simple solvothermal method using cerium nitrate, copper nitrate, and urea as the raw materials, and 1,3,5-benzene-tricarboxylic acid as the ligand for the photocatalytic CO_2 reduction to CO and CH_4. The results show that the built-in electric field constructed by Fermi energy level flattening transfers the electrons in an S-type manner, which not only preserves the strong reducing properties of the electrons in the material but also provides the maximum redox capacity and enables the composite samples to obtain higher visible-light trapping capacity and improve the separation efficiency of the carriers while refining the crystal particles. With the addition of only 1 mL of H_2O as the proton supply source, $CeCu_{0.05}$-BTC/CN exhibits the optimal photocatalytic performance. The CO and CH_4 yields were 64.44 and 0.5575 μmol g^{-1}, which were 7.56 and 2.42 times higher than those of g-C_3N_4, respectively, and the catalytic performances were basically stable after cycling tests.

Received 7th August 2024
Accepted 25th September 2024

DOI: 10.1039/d4ra05721j

rsc.li/rsc-advances

1 Introduction

Since the industrial revolution, the greenhouse effect has become more pronounced as carbon dioxide emissions have continued to increase, and the frequency of extreme weather events has led to increasingly severe global environmental problems.[1,2] The emission of fossil fuels (coal, oil, natural gas, *etc.*) is the main source of the increase of carbon dioxide in the atmosphere.[3] Therefore, it is imperative to reduce the consumption of fossil fuels and the content of carbon dioxide in the atmosphere. Carbon dioxide reduction using solar-driven semiconductor photocatalysts is an efficient and promising technology for achieving long-term solar-fuel conversion.[4,5] Graphite carbon nitride (g-C_3N_4) is a 2D layered semiconductor,[6] which is often regarded as a very promising semiconductor material due to its suitable band gap energy, good chemical-thermal stability, and low cost.[7–9] However, the small specific surface area, the presence of rapid recombination of photogenerated electrons and holes, and the limited absorption and photoresponsivity to visible light limit the practical use of this material for photocatalytic carbon dioxide reduction applications. At present, several aspects of catalyst modification are common in the market, such as chemical doping,[10] the construction of heterojunction,[11] noble metal loading,[12] and the regulation of its morphology.[13] These include metal oxides, sulfides, carbon-nitrides, metal–organic skeletons (MOFs), *etc.*[14,15]

During research in the semiconductor field, MOFs have attracted the attention of a wide range of researchers due to their diverse and controllable crystal structure, ultra-high specific surface area,[16,17] and tunable pores.[18] Cerium (Ce) is an excellent catalytic additive as a rare earth element with unfilled electron 4f orbitals, capable of reversible changes between Ce^{4+} and Ce^{3+}, and surface oxygen vacancy defects that can be spontaneously generated and eliminated. Ye *et al.*[19] obtained oxygen vacancy-rich and N-doped MOF-derived electrocatalysts by pyrolysis of melamine-containing CuCe-BTC with high selectivity and good electrocatalytic activity compared to a reversible hydrogen electrode with a NH_3 yield of 44.5 μg h^{-1} $mg_{cat.}^{-1}$ at 0.5 V. Zhang *et al.*[20] prepared CuO/CeO_2 catalysts synthesized from MOFs using *in situ* synthesis, mechanical mixing, and impregnation methods and found that the CuCeO–ETH catalysts had higher than 98% selectivity for CO oxidation and a wide temperature activity window. Zhang *et al.*[21] achieved efficient CO_2–CH_4 electroconversion with a methane local current density of 138.6 mA cm^{-2} by pyrolysis of a metal–organic framework (MOF) precursor for the preparation of cerium carbide-copper oxide complexes (Cu/CeO_2@C). Therefore, the heterostructured photocatalytic system constructed

[a]*College of Rare-Earth Industry, Inner Mongolia University of Science and Technology, Baotou 014010, China. E-mail: wrf2008@imust.edu.cn*

[b]*Inner Mongolia Key Laboratory of Advanced Ceramic Materials and Devices (Inner Mongolia University of Science and Technology), Baotou 014010, China*

[c]*Key Laboratory of Green Extraction & Efficient Utilization of Light Rare-Earth Resources (Inner Mongolia University of Science and Technology), Ministry of Education, Baotou 014010, China*

from the two may better improve the photocatalyst activity and CO_2 reduction efficiency.

Currently, although some Cu-BTC, Ce-BTC and related materials of CeCu-BTC from different preparation methods have been synthesized, little research has been reported on bimetallic organic frameworks (CeCu-BTC) and graphite carbon nitride (g-C_3N_4) composite heterostructures for photocatalytic carbon dioxide reduction. In the present study, composite heterostructures of bimetallic organic frameworks ($CeCu_x$-BTC) and graphite carbon nitride (g-C_3N_4) were synthesized by a simple solvothermal method using cerium nitrate and urea as raw materials and 1,3,5-benzotricarboxylic acid as a ligand. The results show that Ce-BTC microrods surrounded by Cu-doped microspheres can form beneficial MOFs materials to synergistically improve the photocatalytic CO_2 reduction activity, and this finding also paves the way for further improvement of the photocatalytic CO_2 reduction performance and a small amount of low-cost composite modification of g-C_3N_4.

2 Experimental section

2.1 Materials

Cerium nitrate hexahydrate ($Ce(NO_3)_3 \cdot 6H_2O$), copper nitrate trihydrate ($Cu(NO_3)_2 \cdot 3H_2O$), *N*,*N*-dimethylformamide (C_3H_7NO), 1,3,5-benzene-tricarboxylic acid ($C_9H_6O_6$), all analytically pure AR, Aladdin Reagents Ltd urea (CH_4N_2O), anhydrous ethanol (C_2H_6O), both analytically pure AR, Sinopharm Group Chemical Reagent Co. Ltd acetone (C_3H_6O), analytically pure AR, Tianjin Jindong Tianzheng Fine Chemical Reagent Factory.

2.2 Preparation of g-C_3N_4, Ce-BTC and Cu-BTC

g-C_3N_4 and Ce-BTC were prepared by simple thermal polymerization and solvothermal methods, respectively. The temperature was raised to 550 °C at a rate of 5 °C min^{-1} and held for 4 hours. After grinding, a light yellow g-C_3N_4 powder was obtained.

3 mmol (0.63 g) of 1,3,5-benzene tricarboxylic acid (H_3BTC) and 10 mmol (2.17 g) of $Ce(NO_3)_3$ $6H_2O$ were dissolved in 50 mL (1 : 1) of a mixture of dimethylformamide (DMF) and ethanol, and the mixture was ultrasonicated for 30 min and then sealed in an autoclave at 100 mL, held at 130 °C for 24 h, naturally cooled to room temperature, washed sufficiently, and then dried under vacuum at 80 °C for 12 h. The Ce-BTC powder material was ground. Cu-BTC was prepared by replacing $Ce(NO_3)_3$ $6H_2O$ with 0.13 g of $Cu(NO_3)_2$ $3H_2O$ as described above.

2.3 Preparation of $CeCu_x$-BTC/CN composite photocatalysts

$CeCu_x$-BTC/CN composite photocatalysts were prepared by a simple solvent-thermal method. The $CeCu_x$-BTC/CN composite photocatalysts were prepared similarly to Ce-BTC, except that $Cu(NO_3)_2$ $3H_2O$ and g-C_3N_4 were added to the reaction solution. As an example, $CeCu_{0.05}$-BTC/CN was weighed, and 0.63 g of 1,3,5-benzotricarboxylic acid (H_3BTC), 2.17 g of $Ce(NO_3)_3$ $6H_2O$, and 0.13 g of $Cu(NO_3)_2$ $3H_2O$ were dissolved in a 50 mL (1 : 1) mixture of dimethylformamide (DMF) and ethanol. And 500 mg of g-C_3N_4 was taken in a certain amount of anhydrous ethanol. After ultrasonic dispersion for 30 min, the two were mixed and strongly stirred and sealed in a 100 mL polytetrafluoroethylene stainless steel autoclave at 130 °C for 24 h, naturally cooled to room temperature and centrifuged, washed several times with anhydrous ethanol and acetone, and then vacuum-dried for 12 h at 80 °C and milled to obtain the $CeCu_{0.05}$-BTC/CN powder material. Wherein, the obtained $CeCu_x$-BTC/g-C_3N_4 catalysts were named as $CeCu_{0.05}$-BTC/CN, $CeCu_{0.1}$-BTC/CN, $CeCu_{0.15}$-BTC/CN, $CeCu_{0.2}$-BTC/CN, respectively. CeCu-BTC was prepared with $x = 0.05$ as an example, and in all the synthesised $CeCu_x$-BTC/CN, x denotes a Cu content of 5%.

2.4 Characterization

The crystal structure was analyzed using an X-ray diffraction analyzer with a scanning range of 5 to 70°, Bruker diffractometer type D8-ADVANCE, Germany. GAIA3(XMU/XMH) Ga-ion double beam scanning electron microscope (FIB-SEM) and high-resolution field emission scanning electron microscope Hitachi SU8010 to observe the surface micro-morphology of Czechoslovakia and Japan. Transmission electron microscopy (TEM) images were taken with a FEI-Talos F200S instrument with an accelerating voltage of 200 kV, energy spectrum: X-Twin, origin Netherlands. FT-IR spectrometer to analyze the molecular structure and chemical components of the samples, NICOLET iS50FT-IR type. X-ray electron spectroscopy to analyze the elemental composition and chemical state of the samples, ESCALAB 205Xi type, all of the above are from Thermo Fisher Scientific, USA. UV-Vis Diffuse Reflectance Spectroscopy, test wavelength range 200–800 nm, Model U-3900, Hitachi High-Technologies Corporation, Japan. PL Fluorescence Spectroscopy, testing wavelength of 285 nm, Model F-4600, Hitachi High-Technologies, Japan. Beijing Perfectlight High Performance Xenon Light Source simulating daylight (PLS-SXE300E/UV), power 300 W, Beijing Perfectlight Technology Co. Fully automated system gas chromatography for photocatalytic carbon dioxide reduction testing, Model GC79720, Beijing CEC Jinyuan Technology Co. Electrochemical workstation for electrochemical performance testing of samples, Model 1260A+1287A, Sully Strong, UK. EPR electron paramagnetic resonance spectrometer using the Bruker model E500, Germany.

2.5 Photocatalytic CO_2 reduction

The photocatalytic CO_2 reduction experiments were carried out in a sealed 250 mL quartz glass reactor with a 28# standard ball mill and flange O-ring seal, which was connected to an automatic on-line photocatalytic analysis system using a PLS-SXE300 xenon lamp with a wavelength of 320–780 nm as the light source. Specifically, 50 mg of photocatalyst was put into the reaction bottle to build a platform, and 1 mL of deionized water was used as the reaction solution. Before illumination, vacuum the reaction system 2–3 times until the pressure gauge shows −91.7 kPa, and then charge pure CO_2 gas with high-purity argon as the carrier gas. Use the circulating water

chiller to maintain the temperature in the bottle and carry out the photocatalytic reaction under stable temperature conditions. The trace gas in the reaction bottle was extracted by automatic sampling every 60 min, and the yield of CO and CH_4 was obtained by a GC7920 gas chromatograph (equipped with FID, TCD, ECD, and FPD detectors).

2.6 Electrochemical testing

The electrochemical tests were carried out using a three-electrode system. Glymercury electrode was used as a reference electrode, a platinum electrode as a counter electrode, a catalyst membrane electrode as a working electrode, and a 0.2 mol L^{-1} Na_2SO_4 aqueous solution as an electrolyte. Catalyst membrane electrode: 10 mg of photocatalyst was weighed and mixed with 0.2 mL of ethanol, 0.7375 mL of water, and 0.0625 mL of 5% Nafion solution and sonicated for at least 30 min, Next, using a micropipette, 10 μL of the combined solution was applied to a 4 cm^2 conductive glass surface, creating a center area with a volume of 1 cm^2, which was then left to dry naturally. The transient photocurrent test potential in the photocurrent test was 0.1 V, and the test time was 540 s with a light–dark cycle of 60 s. Electrochemical impedance frequency range 100 kHz to 0.01 Hz.

2.7 Electron paramagnetic resonance (EPR)

5,5-Dimethyl-1-pyrroline-N-oxide (DMPO) was used as a spin trapping agent and methanol as a hole-sacrificing agent at room temperature and atmospheric pressure. Mix the solution to be tested with 100 mm of capturing agent in a ratio of 1 : 1 to obtain 1 mL of the mixed solution. After full mixing, suck 30 μL with a capillary glass tube and put it into the EPR-specific test tube. Record the spectral signal in dark and light conditions for 15 minutes.

3 Results and discussion

3.1 Characterization of physical phases and micromorphology

Fig. 1(a–c) shows the XRD spectra of the samples, the bright diffraction peaks of the samples indicate that all the samples are well crystallized. There are two distinct diffraction peaks at 13.05° and 27.34° for g-C_3N_4, corresponding to the (100) and (002) crystal planes of the graphite-like phase, respectively, which are attributed to the in-plane stacking and interlayer stacking of the typical triazine ring in g-C_3N_4 (ref. 22) (JCPDS 87-1526), The stronger diffraction peak crystal spacing is typically 0.326 nm. The diffraction peaks of Ce-BTC were 8.5°, 10.6°, and 18.1°, respectively, and the XRD data were consistent with the previous report[23] (CCDC ID: 773084), in which the peaks of CeCu-BTC and Ce-BTC remained consistent. It is noteworthy that a part of CeO_2 was generated in the samples under hydrothermal conditions, with diffraction peaks of 28.55°, 33.09°, and 47.49°, corresponding to the (111), (200), and (220) crystal planes of CeO_2, respectively. The Cu-BTC diffraction peaks were 6.7°, 9.5°, 11.6°, 13.5°, and 19.3°, respectively. Some of the synthesised samples contain very small amounts of

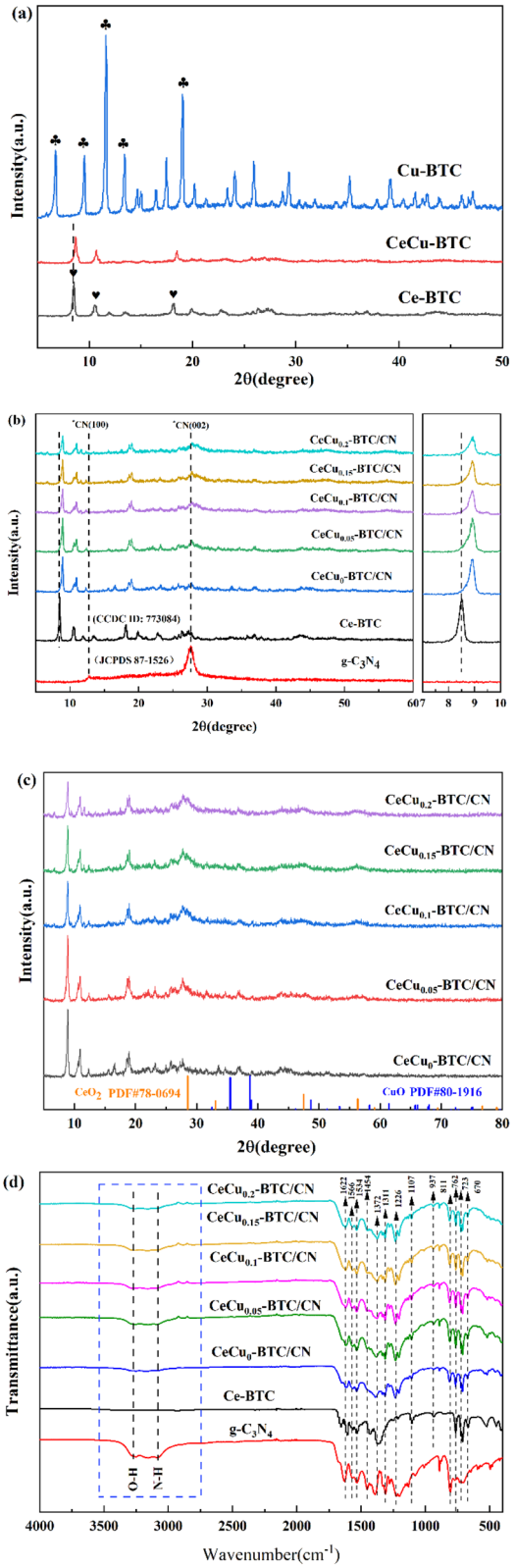

Fig. 1 XRD patterns of Ce-BTC, Cu-BTC and CeCu-BTC (a), g-C_3N_4, Ce-BTC and $CeCu_x$-BTC/CN (b), XRD spectra of CeO_2 and CuO (c), FT-IR spectra of g-C_3N_4, Ce-BTC and $CeCu_x$-BTC/CN (d).

copper oxide impurities, and the diffraction peaks at 35.5° and 38.9° correspond to the (111) and (200) crystal planes of CuO, respectively.[19,20] Due to the difference between the ion radii of Ce^{3+} (1.02 A) and Cu^{2+} (0.73 A), the doping of Cu causes the XRD pattern to move in a higher 2θ direction, indicating that the nodes of the Ce^{3+} skeleton are partially and isomorphically replaced by Cu^{2+} ions to form CeCu-BTC. With the increasing amount of Cu doping in the heterojunction, the corresponding (101) diffraction peak intensity gradually decreases, the full width of the half-peak increases, and the grain size gradually decreases, indicating that the crystal growth process of Ce-BTC is hindered by the high content of Cu,[24] and the refined grain size also helps to increase the specific surface area of the composite photocatalyst, which in turn improves its photocatalytic performance.

Fig. 1(d) shows the FT-IR spectra of the samples, and all $CeCu_x$-BTC/CN samples show almost the same absorption bands, and the broad absorption bands at 3500–2820 cm^{-1} can be attributed to the bonded or physically adsorbed hydroxyl (–OH) stretching vibrations of the bonded or physically adsorbed water molecules and the N–H bond stretching vibrations.[25] In the characteristic frequency region, the absorption bands at 1625–1534 cm^{-1} and 1454–1372 cm^{-1} belong to the asymmetric stretching vibration (vas) and symmetric stretching vibration (vs) of the carboxyl group (O–C=O) in homobenzoic acid,[26,27] respectively. In the fingerprint region, the absorption bands at 1300–1000 cm^{-1} belong to C–O stretching vibration, the absorption band at 1107 cm^{-1} corresponds to C–H in-plane bending vibration, and the absorption peak at 810 cm^{-1} corresponds to the out-of-plane bending vibration of the heptane-triazole ring in g-C_3N_4. It is also found that the absorption intensity of the peak at this location gradually increases with the increase of Cu content in the heterojunction. The absorption bands at 767 and 721 cm^{-1} correspond to C–C ring out-of-plane bending vibrations, which confirm the aromatic ring structure of the BTC ligand.[28] The absorption band between 700 and 450 cm^{-1} can be attributed to the Ce–O stretching vibration of Ce-BTC samples.

By comparison, it can be seen that the organic ligand BTC has formed a bridge structure with rare earth ions and Cu ions. For the offset phenomenon of some absorption peaks, it also shows that the compound of BTC and g-C_3N_4 has a significant impact on the chemical environment of the g-C_3N_4 molecule, which fully shows that the two have successfully constructed a heterojunction, which is consistent with the XRD analysis results.

Fig. 2 is the SEM image of the sample. Fig. 2(a) shows that g-C_3N_4 presents a clearly visible irregular two-dimensional folded layered structure, and the adjacent thin sections may show a good pore structure.[29] Ce-BTC in Fig. 2(b) shows a typical rod- or bar-like structure with different sizes and lengths, mostly around 15–20 μm, presenting a smooth and textured surface, and the crystal edges can be clearly seen. Fig. 2(c) shows the tight and ordered stacking of Ce-BTC and g-C_3N_4 cladding after the sonicated g-C_3N_4 structure has been dispersed. Some surface aggregates of copper oxide with microspherical structure and micron flower-like g-C_3N_4 are shown in Fig. 2(d). In addition, when the Cu content was further increased, such as in $CeCu_{0.1}$-BTC/CN samples, more Cu-BTC particles appeared (Fig. 2(h)), but the high content of Cu caused the crystal growth of Ce-BTC to be hindered, which might lead to a corresponding decrease in the particle size of Cu-BTC (Fig. 2e–g).[30] To sum up, Cu-BTC and g-C_3N_4 are evenly dispersed in the structure of Ce-BTC to form a relatively complex structure. It is inferred that heterostructures may be formed and play a certain role in promoting the separation of charges in photoexcitation.[31]

Fig. 3 shows the TEM image of the sample, and Fig. 3(a) shows that some coalesced spherical Cu-BTC and rod-shaped Ce-BTC are uniformly distributed on the smooth carbon nitride surface and are in close contact on the surface of g-C_3N_4, Further, it is clearly proved that Cu in Ce-BTC is successfully doped and coexists with g-C_3N_4, forming a more complex structure, which proves that the sample is successfully compounded. As reported in previous studies, g-C_3N_4, with its functional amino groups and large specific surface area, is also a good carrier for loading nanocatalysts, which is more favorable for the construction of heterojunction[32,33] structure. Thus, in summary, it was confirmed that the $CeCu_x$-BTC/CN composite heterojunction was successfully constructed, and the composition of this heterojunction may be conducive to the rapid transfer of photoexcited electrons at the interface,[34] which may improve charge migration and photocatalytic efficiency. Fig. 3(b and c) clearly show lattice spacings of 0.32, 0.31, 0.19, and 0.21 nm corresponding to the (002) crystallographic plane of g-C_3N_4, the (111) and (220) crystallographic planes of CeO_2, and the (200) crystallographic plane of CuO grains, with well-matched lattice planes and good agreement with the XRD data. Fig. 3(d) shows its dark field image. By collecting scattered (diffracted) electronic signals for imaging, it can be seen that the larger and thicker the sample, the stronger the scattering and the brighter the sample area in the dark field. Fig. 3(e–h) clearly shows the elemental distribution of the samples, with brighter points in the elemental mapping region indicating higher concentrations of the matched elements. It is worth noting that the distribution of C, N, O, Ce, and Cu elements is relatively uniform. The total distribution of each element is shown in Fig. 3(i), which indicates the good coexistence of Ce-BTC, Cu-BTC, and g-C_3N_4, and it also indicates that the structure of the prepared samples is well dispersed and thermally stable, and it also proves once again that the samples are successful in constructing heterojunctions.

Fig. 4 shows the surface element and chemical valence composition of g-C_3N_4, CeCu-BTC, and $CeCu_{0.05}$-BTC/CN. Pollution carbon (284.8 eV) was selected as the internal standard for all elements in the figure, and the spectral correction has been completed. Fig. 4(a) shows the full spectrum of the sample. It is found that there are mainly energy spectrum peaks related to C 1s, N 1s, and O 1s elements in g-C_3N_4. CeCu-BTC and $CeCu_{0.05}$-BTC/CN mainly have energy spectrum peaks related to C 1s, N 1s, O 1s, Ce 3d, and Cu 2p elements without other impurities, which corresponds to XRD data. The element content in $CeCu_{0.05}$-BTC/CN also indicates that g-C_3N_4 and $CeCu_x$-BTC are successfully combined.

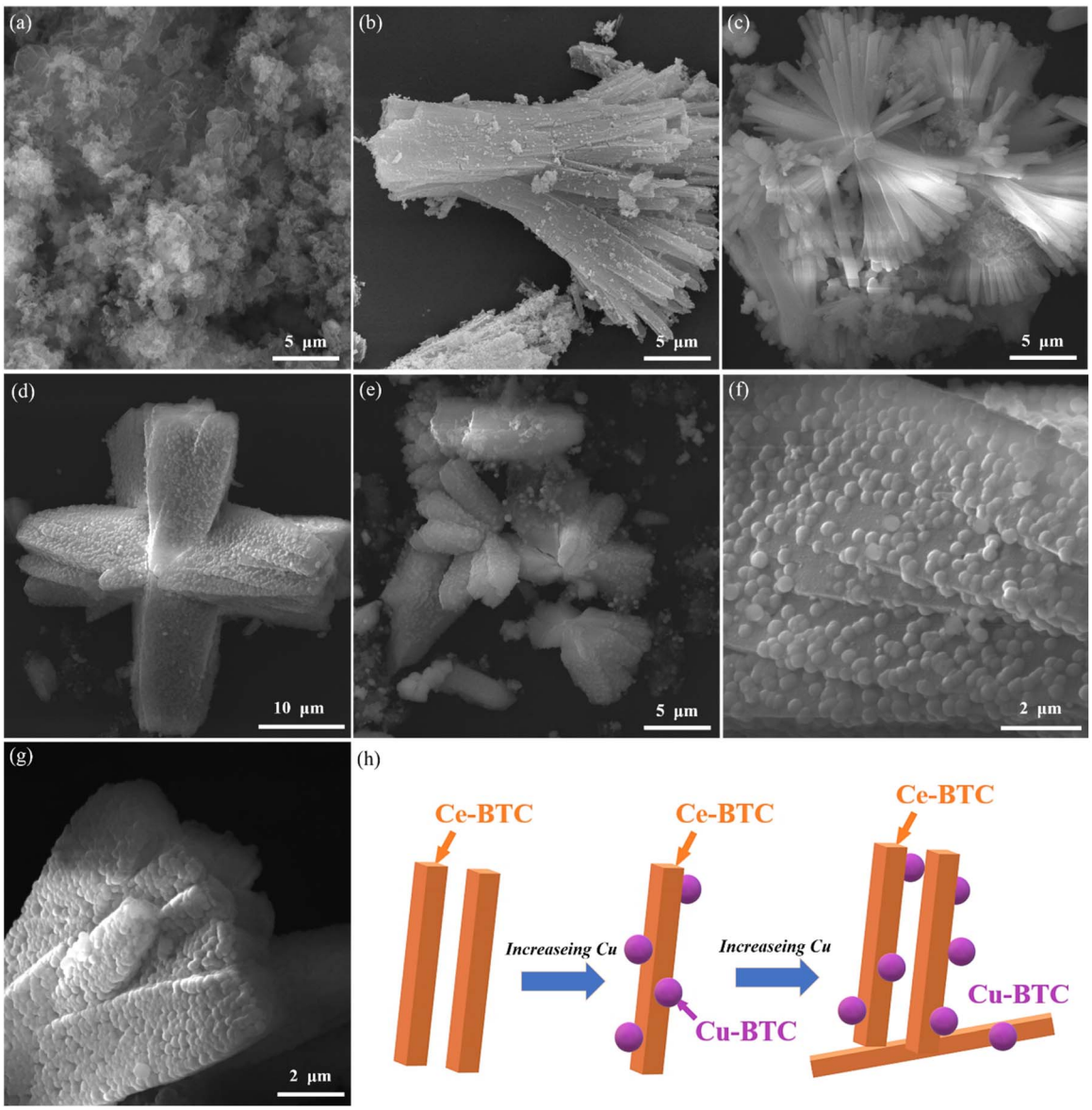

Fig. 2 SEM images of g-C_3N_4 (a), Ce-BTC (b), $CeCu_0$-BTC/CN (c), $CeCu_{0.05}$-BTC/CN (d), $CeCu_{0.1}$-BTC/CN (e), $CeCu_{0.05}$-BTC/CN sample enlarged view (f), $CeCu_{0.1}$-BTC/CN sample enlarged view (g), schematic diagram of sample crystal growth (h).

As shown in Fig. 4(b), the C 1s spectrum is deconvoluted into three characteristic peaks, of which the characteristic peak of 284.8 eV corresponds to the amorphous carbon (C–C) of the sample, and the characteristic peaks at 285.7 eV and 288.12 eV correspond to C–O–C and C–C=O[35,36] respectively. The characteristic peak at 287.84 eV corresponds to the characteristic peak of SP^2 hybridized carbon in g-C_3N_4 (N–C=N),[19] The peak is shifted by 0.28 eV to reach 288.12 eV at high binding energy in the composite samples, suggesting that there is a change in charge transport or chemical environment at the surface of the triazine ring, which may be related to the introduction of $CeCu_x$-BTC, and also indicates that the density of the electron cloud around the Ce and Cu atoms is increased. Fig. 4(c) shows that the peak of the N 1s energy level appears at the C–N binding energy of 398.35 eV, which corresponds to the pyridine nitrogen in the tricycle (C=N–C) shown in Fig. 4(d) at binding energies of 529.6 eV, 531.63 eV, and 533.1 eV, respectively, can be classified into three component peaks: lattice oxygen (Olat), surface chemisorbed oxygen (OAds), and surface reactive oxygen (OSur), which correspond positively to C=O and C–O.[19,36] Among them, surface active oxygen (OSur) is mainly classified as metal oxide-bonded (Cu–O or Ce–O), which is derived from oxygen defects with lower coordination properties or weaker surface oxygen bonding and possesses better oxidative activity against toluene at low temperatures,[37,38] so it is speculated that the fabricated samples may possess better catalytic activity. As an example, Ce 3d of CeCu0.05-BTC/CN in Fig. 4(e). The Ce 3d spectrum is deconvoluted into two spin–orbit peaks v and u and assigned to Ce $3d_{3/2}$ *vs.* Ce $3d_{5/2}$. Notate v^0 (882.5 eV), v′ (885.7 eV), v″ (888.4 eV), v‴ (898.1 eV), u^0 (900.6 eV), u′ (903.9 eV), u″ (906.7 eV), u‴

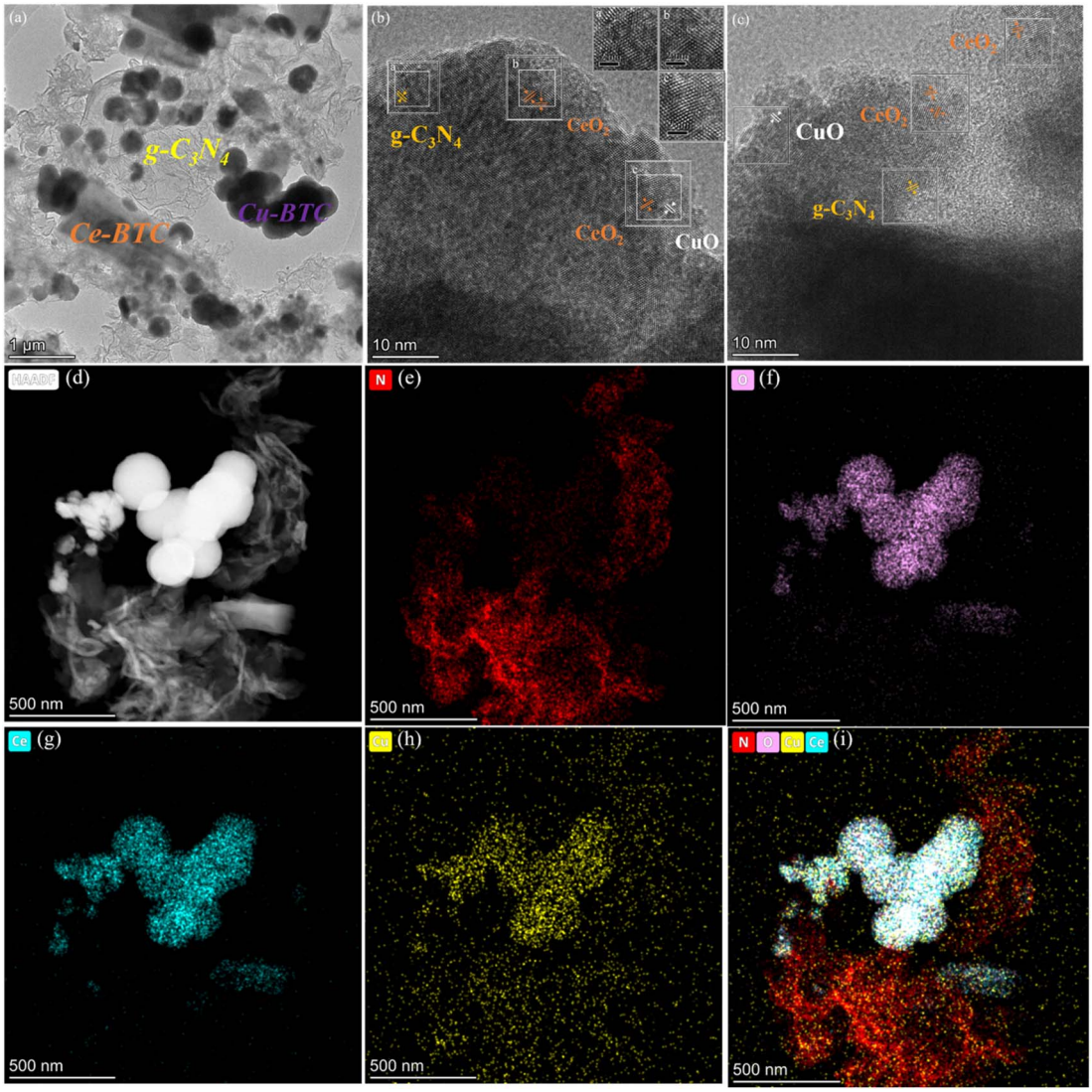

Fig. 3 TEM (HR-TEM) (a–c) of $CeCu_{0.05}$-BTC/CN, dark field image of $CeCu_{0.05}$-BTC/CN (d), EDS mapping image: N (e), O (f), Ce (g), Cu (h), general diagram of element distribution (i).

(916.7 eV). The four characteristic peaks u^0, u′, u″, and u‴ are attributed to Ce $3d_{3/2}$ spectral peaks, and v^0, v′, v″, and v‴ are attributed to Ce $3d_{5/2}$ spectral peaks. u^0, u″, and u‴ with v^0, v″, and v‴ can be attributed to Ce^{4+}, and the remaining two characteristic peaks correspond to Ce^{3+}.[20,30,38] Therefore, Ce^{3+} and Ce^{4+} coexisted on the surface of this sample, and it was hypothesized that the abundant photocatalytic properties could also be attributed to the renewable conversion between Ce^{3+} and Ce^{4+}. In Fig. 4(f), the Cu 2p spectrum is deconvoluted into two spin orbital peaks, Cu $2p_{3/2}$ and Cu $2p_{1/2}$, corresponding to binding energies of 933.1, 934.3 eV, and 952.5, 956.3 eV (ref. 19 and 20) respectively. The Cu element in $CeCu_x$-BTC mainly exists in the form of Cu^+ and Cu^{2+}, while the peaks of Ce 3d and Cu 2p are shifted in the direction of low binding energy, which indicates that there are interactions and electron transfer between CeCu-BTC and g-C_3N_4. It indicates that the photogenerated electrons on the g-C_3N_4 surface are transferred to CeCu-BTC, and the electron–hole pair complex is effectively suppressed. This is in agreement with the XRD and TEM data.

Fig. 5(a and b) shows the UV-Vis absorption spectra of the samples in the range of 250–800 nm, which were calculated using the Tauc plot algorithm and the energy band eqn (1).

$$\alpha h\nu^{1/n} = A(h\nu - E_g) \quad (1)$$

where α is the absorbance index, n is determined by the type of optical jump within the semiconductor, ν is the frequency, h is Planck's constant ($4.1356676969 \times 10^{-15}$), and E_g is the semiconductor bandgap width. Apparently, $CeCu_{0.05}$-BTC/CN shows a significant enhancement of visible light absorption compared to g-C_3N_4, while the presence of heterojunction results in red-shifted absorption bands, suggesting that the sample is capable of attracting more visible-light photons in the UV and visible ranges to obtain the active e^-/h^+, which subsequently

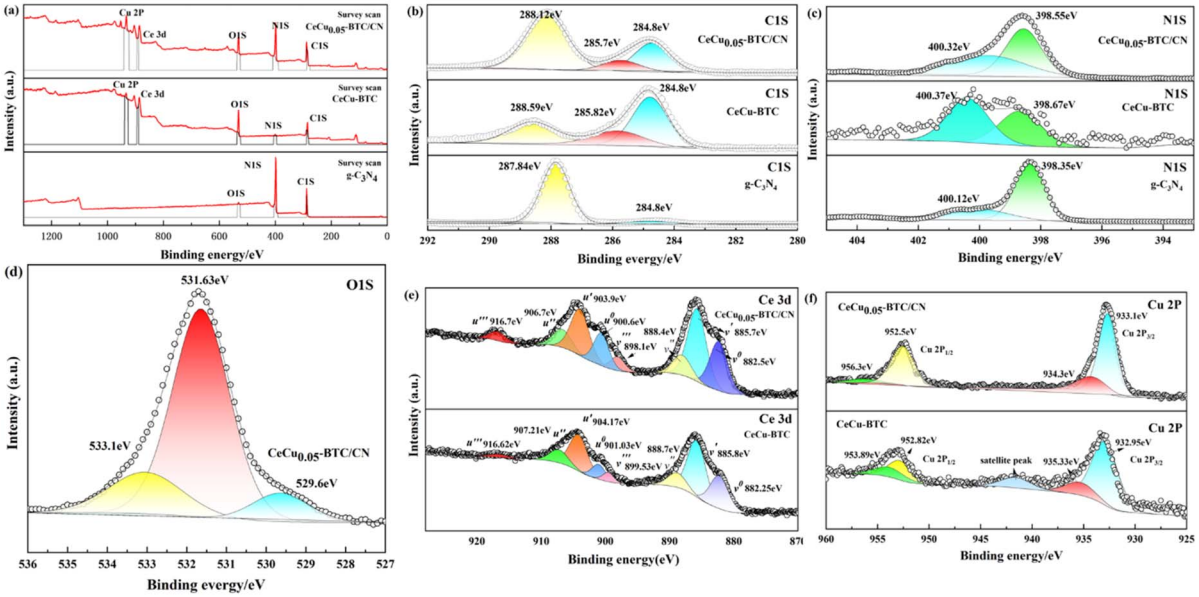

Fig. 4 XPS spectra of the g-C_3N_4, CeCu-BTC and $CeCu_{0.05}$-BTC/CN: total elemental spectra (a), C 1s (b), N 1s (c) O 1s (d), Ce 3d (e), Cu 2p (f).

improves the photocatalytic performance. As shown in Fig. 5(a and b), the visible absorption band edges of g-C_3N_4, CeCu-BTC and, $CeCu_{0.05}$-BTC/CN are about 455 nm, 534 nm, and 509 nm, which is in agreement with earlier reports.[39] The optical band gap energy (E_g) valuations of 2.72, 2.32, and 2.44 eV for g-C_3N_4, CeCu-BTC, and $CeCu_{0.05}$-BTC/CN, respectively, were deduced from eqn (1). The results show that the introduction of Cu narrows the optical band gap value of $CeCu_{0.05}$-BTC/CN composites, and the lower E_g values indicate that the samples may produce more photogenerated carriers and possess higher visible light trapping ability.[34]

Fig. 5(c) shows the separation of photogenerated carriers generated at the contact interface of different samples at the 315 nm excitation wavelength. The stronger the PL peak, the higher the e^-/h^+ recombination rate, and the lower the corresponding separation efficiency, which is more conducive to the photocatalytic reaction. This is also one of the reasons why the original g-C_3N_4 has low capture ability for visible light and is

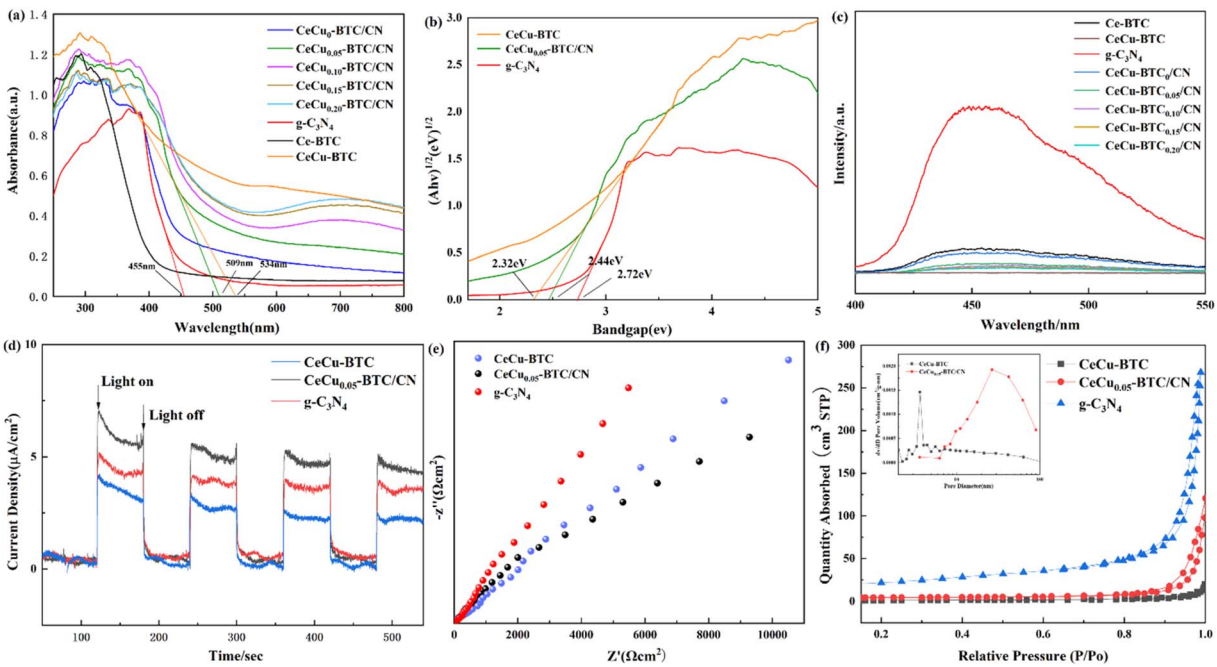

Fig. 5 UV-Vis absorption spectrum (a) and Tauc curve (b), fluorescence spectrum (c), transient photocurrent response spectrum (d), Nyquist plots (e) of the sample, N_2 adsorption and desorption isothermal curves and pore size distribution curves (f).

easy to compound. CeCu-BTC has no fluorescence in this band, which also shows that the introduction of the metal organic framework helps to reduce the carrier recombination. At the same time, it is speculated that the phenomenon of improving the photoelectron separation efficiency and reducing the recombination rate should also be related to the synergistic effect between g-C_3N_4 and Cu doping in CeCu-BTC and Ce.[30] In summary, the construction of this heterojunction not only enhances the photoelectron transport capacity but also effectively suppresses the recombination rate and, at the same time, has a contributing effect on the improvement of photocatalytic performance.[40,41]

Fig. 5(d) shows the transient current response of CeCu-BTC, $CeCu_{0.05}$-BTC/CN, and g-C_3N_4. The intensity of the photocurrent reflects the separation efficiency of photogenerated electrons and holes.[42] The transient photocurrent intensity of $CeCu_{0.05}$-BTC/CN was significantly higher than that of CeCu-BTC, and g-C_3N_4, showing a periodic and stable reciprocating law, indicating that the carrier separation efficiency in the synthesized heterostructure is higher and the photocatalytic reaction is more efficient. The radius of the arc area in the EIS Nyquist plot shown in Fig. 5(e) indicates the resistance to the transfer of charge on the surface of the semiconductor electrode.[43] With the decrease in semicircular radius, the generation efficiency of electron hole pairs increases. It is observed that the arc radius of $CeCu_{0.05}$-BTC/CN Nyquist is smaller than that of other samples, which indicates that the former has a smaller transmission impedance and lower resistance to carrier separation, which is more conducive to charge transfer. Fig. 5(f) shows the N_2 adsorption–desorption experiments of the samples at 77 K. The g-C_3N_4, CeCu-BTC, and $CeCu_{0.05}$-BTC/CN were found to be H_3-type hysteresis loops with type IV adsorption isotherms. When the sample is at P/P_0 >0.8, the hysteresis loop may be due to the adsorption of N_2 in the slit pores of MOFs, and the H_3 hysteresis loop is mainly found in the aggregates of layered structure, so it is speculated that it may be the intermolecular graphite-like structure of g-C_3N_4. This type of hysteresis loop also shows that most of the materials have a mesoporous structure and the pore distribution is uneven. The specific surface area, pore volume, and average pore size of different samples can be obtained in Table 1. It is found that the specific surface area and average pore size of $CeCu_{0.05}$-BTC/CN are significantly increased compared with CeCu-BTC. It is inferred that the doping of Cu and the recombination of g-C_3N_4 may lead to more defects and affect the growth of crystals, which is also consistent with the results of electron microscopy. At the same time, we infer that a more porous structure and relatively large specific surface area also provide more active sites and the possibility of reagent adsorption for the reaction, thereby enhancing the photocatalytic ability of the sample.

Table 1 Comparison of S_{BET}, pore volume and average pore size

Sample	S_{BET} ($m^2\ g^{-1}$)	Pore volume ($cm^3\ g^{-1}$)	Average pore size (nm)
g-C_3N_4	73.87	0.41	22.40
CeCu-BTC	4.4905	0.03	26.04
$CeCu_{0.05}$-BTC/CN	16.510	0.13	35.53

3.2 Photocatalytic carbon dioxide reduction

Fig. 6 shows the photocatalytic reduction test of carbon dioxide under simulated sunlight. g-C_3N_4 and $CeCu_x$-BTC/CN products are both CO and CH_4, where CO is designated as the main product, accompanied by a small amount of methane production. The photocatalytic carbon dioxide reduction experiments were carried out under gas–solid phase conditions with 1 mL of pure water as the proton-providing source and no sacrificial agent, and the reaction mechanism of the different intermediates produced by participating in the carbon dioxide reduction can be represented by the following reaction equations.[44]

$$H_2O + h^+ \rightarrow {}^{\bullet}OH + H^+$$

$$2CO_2 + 4e^- + 4h^+ \rightarrow 2CO + O_2$$

$$CO + 6e^- + 6H^+ \rightarrow CH_4 + H_2O$$

For the original g-C_3N_4, the CO yield is only 8.522 μmol g^{-1} and the CH_4 yield is 0.232 μmol g^{-1} under this condition, which may be due to the higher charge-carrier recombination rate and rapid recombination. As can be seen in Fig. 6(a), the CO and CH_4 reduction capacities of $CeCu_x$-BTC/CN, which successfully constitutes the heterostructure, are both higher than those of g-C_3N_4. Among them, $CeCu_{0.05}$-BTC/CN CO yield was 64.44 μmol g^{-1}, which was 7.56 times of g-C_3N_4, and the CO yields of other samples were 15.07, 36.39, 34.43, and 31.07 μmol g^{-1} ($x = 0$, 0.1, 0.15.0.2), which were 1.77, 4.27, 4.04, and 3.65 times of g-C_3N_4, respectively. The yield of the heterostructure $CeCu_{0.05}$-BTC/CN shown in Fig. 6(b) was 0.5575 μmol g^{-1}, which was 2.42 times higher than that of g-C_3N_4, and the CH_4 yields of the other samples were 1.149, 0.557, 0.552, and 0.542 μmol g^{-1} ($x = 0$, 0.1, 0.15, 0.2), which were 5 times higher than that of g-C_3N_4, respectively, 2.42, 2.4, and 2.36 times that of g-C_3N_4, respectively. It also shows that the content of Cu doping is the key to realizing the high photocatalytic activity of the composite heterostructure material. The suitable Cu content makes it well dispersed on Ce-BTC and g-C_3N_4 surfaces, which facilitates carrier transfer and separation.[45,46] In addition, when the content of Cu was higher than 5.0 wt%, a further increase in the proportion of Cu led to a decrease in the photocatalytic CO_2 reduction performance.

Fig. 6(c) shows that in the absence of a photocatalyst, light source, or N_2 atmosphere instead of CO_2, the reaction did not produce CO and CH_4, indicating that CO_2 was the only carbon source involved in the reduction reaction, with no other factors influencing it. Fig. 6(d) shows the cycling test of sample $CeCu_{0.05}$-BTC/CN, in which the CO and CH_4 yields were found to remain good after centrifugal recovery and activation several times. In addition, the recovered XRD spectra (Fig. 6(e)) and FT-IR spectra (Fig. 6(f)) also proved that the main crystal structure and chemical functional groups had no obvious change after the stability test, indicating that it had good photocatalytic stability.

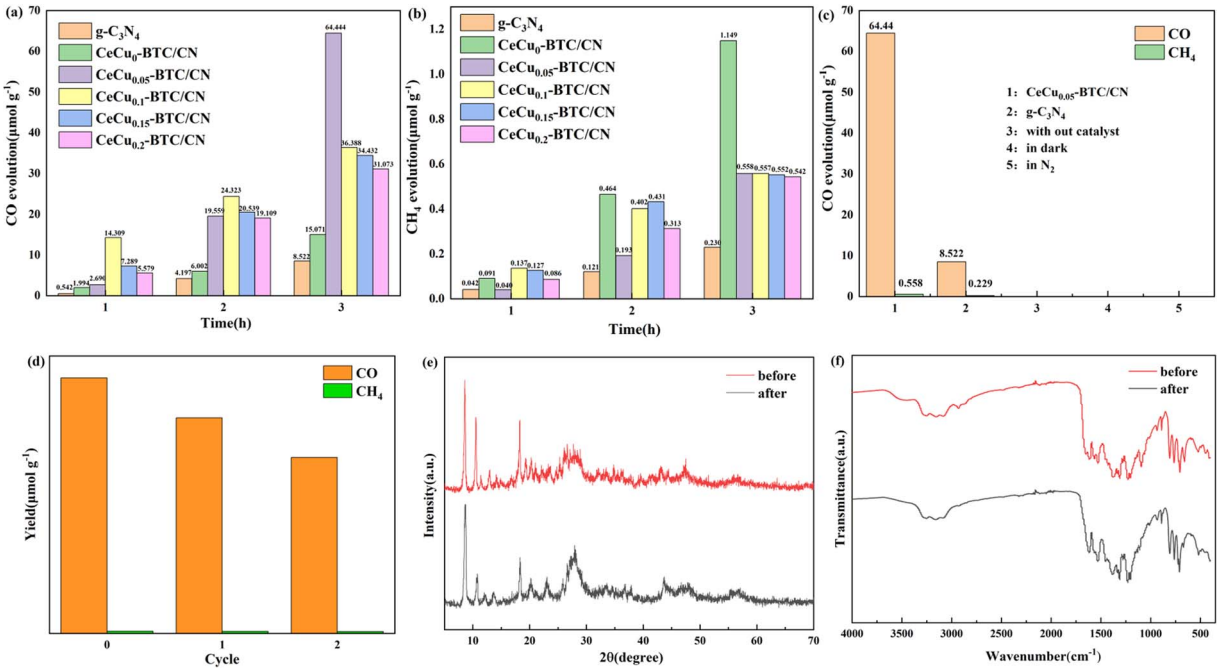

Fig. 6 Photocatalytic CO_2 reduction CO yield plot (a), CH_4 yield plot (b), control experiment (c), $CeCu_{0.05}$-BTC/CN cycle test (d), XRD and FT-IR changes of the samples before and after illumination (e and f).

3.3 Research on photocatalytic mechanism

To further explain the sample mechanism, electron paramagnetic resonance (EPR) was used to analyze the direction of electron transfer in the system. In Fig. 7(a and b), DMPO-˙OH was not seen in any of the dark reaction conditions, and $CeCu_{0.0.5}$-BTC and $CeCu_{0.0.5}$-BTC/CN were observed in the light reaction, showing a standard fourfold peak and four peaks equidistant with peak heights of 1 : 2 : 2 : 1. The larger DMPO-˙OH may be attributed to its VB potential to be corrected, that is, the VB potential of CeCu-BTC and $CeCu_{0.05}$-BTC/CN should be greater than 1.99 eV (ref. 47) (OH^-/–OH 1.99 eV). On the contrary, DMPO-˙OH was not found in g-C_3N_4, presumably due to the weak oxidation potential of the photogenerated holes, which also suggests that the photogenerated holes remain in the VB of CeCu-BTC and are not transferred to the VB of g-C_3N_4. According to the linear extrapolation results, the $E_{VB\text{-}XPS}$ of g-C_3N_4 and CeCu-BTC in Fig. 7(c and d) are 1.65 and 2.03 eV, respectively.

In order to obtain the actual VB potential of the samples more accurately and efficiently, the samples were estimated according to eqn (2) and (3). φ is the work function of the XPS instrument, with a value of 4.2 eV, and the NHE at pH = 7 is 4.44 eV. As a result, the values of $E_{VB\text{-}NHE}$ for g-C_3N_4 and CeCu-BTC are obtained as 1.41 and 1.79 eV. Eqn (3) yields ECB's of −1.31 and −0.53 eV for g-C_3N_4 and CeCu-BTC, respectively.

$$E_{VB\text{-}NHE} = \varphi + E_{VB\text{-}XPS} - 4.44 \quad (2)$$

$$E_{CB} = E_{VB} - E_g \quad (3)$$

Finally, to verify the accuracy of the above potential calculations, we also utilised the semiconductor electronegativity theory (shown in eqn (4)) to calculate the VB potential. X is the geometric mean of the absolute electronegativity of the atoms within the semiconductor, and E_c is a constant with respect to

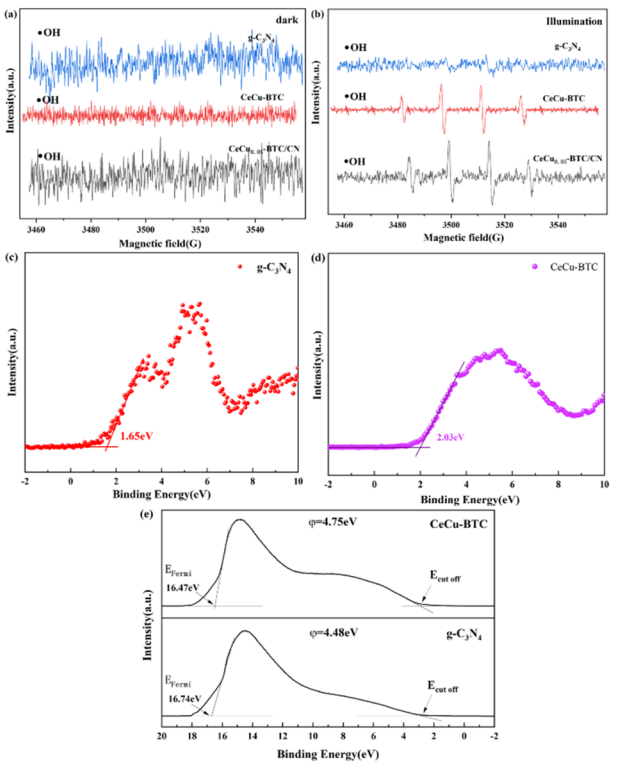

Fig. 7 EPR spectra of DMPO-˙OH spin capture (a and b), VB-XPS (c and d), UV electron spectroscopy UPS (e).

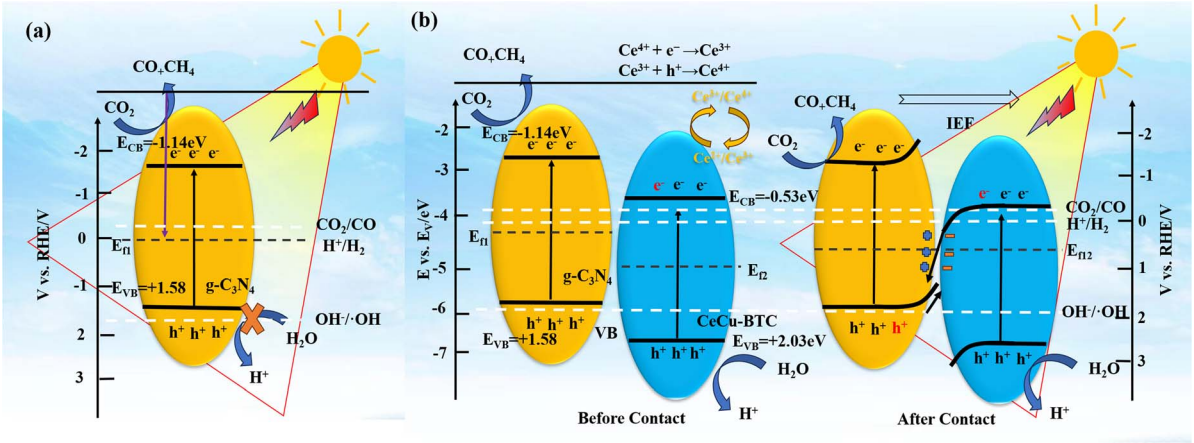

Fig. 8 Photocatalytic mechanism diagram of g-C_3N_4 (a), the work functions of CN and CeCu-BTC before/after contact and the formation of internal electric field (b).

the standard H electrode, generally taken to be 4.5 eV, with X for g-C_3N_4 being 4.73 eV,[48] as an example. The E_{VB} of g-C_3N_4 is 1.58ev and the E_{CB} is −1.14. Meanwhile, the results obtained by the two calculation methods were found to be approximate, and the semiconductor electronegativity theory was further used for the explanation of the photocatalytic mechanism.

$$E_{VB} = X - E_e + 0.5E_g \quad (4)$$

$$\varphi = 21.22 - \Delta E \quad (5)$$

In addition, Fig. 7(e) shows the ups spectrum of the sample. The work function (φ) of the sample is obtained through formula (5), and ΔE is the distance from the upper starting point to the cut-off edge of the secondary electron after the bias voltage is applied. The φ of g-C_3N_4 and CeCu-BTC are 16.74 and 16.47 eV, respectively. The results indicate that CeCu-BTC has a larger φ value and a relatively small Fermi energy level, while the opposite is true for g-C_3N_4. Therefore, when g-C_3N_4 and CeCu-BTC are in close contact to form a CeCu-BTC/CN heterojunction, the work function difference between the two samples causes the free electrons of CN to spontaneously transfer to CeCu-BTC. With the Fermi level of g-C_3N_4 gradually decreasing, the Fermi level of CeCu-BTC gradually increases until the interface Ef_{12} reaches equilibrium. Similarly, a space charge region, *i.e.* an built-in electric field, will be formed at the interface between the two. The existence of the built-in electric field will bend the Fermi level and pull up the energy band of g-C_3N_4 and lower the energy band of CeCu-BTC. Therefore, the photogenerated electrons of g-C_3N_4 have to overcome the potential energy barrier to fall back into CeCu-BTC driven by the built-in electric field and interface chemical bonds (Fig. 8(a and b)). Finally, by analyzing the photocatalytic CO_2 reduction mechanism diagram of g-C_3N_4 and the electron paramagnetic resonance (EPR) capture results of hydroxyl radicals (·OH) shown in Fig. 7(a), And combined with the position where the energy bands of the photocatalysts are located, it is preferred that the photogenerated electrons on the CB of CeCu-BTC will recombine with the photogenerated holes of the VB of g-C_3N_4, which also verifies the successful construction of the S-type heterojunction.

The above conclusions indicate that CeCu-BTC and CN change from a steady state to an excited state upon irradiation with visible light larger than the bandgap of both, producing photogenerated electrons and holes. Due to the interaction of IEF and Coulomb at the interface, the photogenerated electrons on the CB of CeCu-BTC will combine with the photogenerated holes on the VB of g-C_3N_4, and then the photogenerated electrons accumulated on the CB of g-C_3N_4 will react with the CO_2 adsorbed on the surface of the catalyst to form CO and CH_4. Meanwhile, the CB potential of CeCu-BTC and g-C_3N_4 is more negative than that of Cr(VI)/Cr(III) (+0.51 EV *vs.* NHE), which indicates that the reduction of adsorbed Cr(VI) to Cr(III) is thermodynamically beneficial to the CB of the photocatalyst. The coexistence of Ce^{3+} and Ce^{4+} can also aid in the transfer of electrons from the catalyst surface, thus prolonging the reaction time between electrons and carbon dioxide.

4 Conclusions

In summary, The S-type heterojunction photocatalysts ($CeCu_x$-BTC/CN) with cerium-copper bimetallic organic framework ($CeCu_x$-BTC) and graphite-phase carbon nitride (g-C_3N_4) were constructed by a simple solvothermal method for photocatalytic CO_2 reduction to CO and CH_4. The results show that the built-in electric field constructed by Fermi energy level flattening transfers the electrons in an S-type manner, which not only preserves the strong reducing properties of the electrons in the material but also provides the maximum redox capacity and enables the composite samples to obtain higher visible-light trapping capacity and improve the separation efficiency of the carriers while refining the crystal particles. $CeCu_{0.05}$-BTC/CN possessed the optimal photocatalytic performance with the addition of only 1 mL of H_2O as the proton provision source. The CO and CH_4 yields were 64.44 μmol g^{-1} and 0.5575 μmol g^{-1}, which were 7.56 and 2.42 times higher than that of g-C_3N_4, respectively, and the catalytic performance was basically stable after the cyclic test,

and this heterojunction also paved the way for a small amount of low-cost composite modification of g-C_3N_4.

Data availability

Crystallographic data for g-C_3N_4,Ce-BTC, have been deposited at the JCPDS/CCDC under JCPDS 87-1526, CCDC ID: 773084 and can be obtained from **http://dx.doi.org/10.1002/smll.202003597**, **https://doi.org/10.1016/j.matchemphys.2018.04.031**, **http://dx.doi.org/10.1016/j.apsusc.2017.06.235**. The authors confirm that the data supporting the findings of this study are available within the article and/or as its supplementary materials. The data that support the findings of this study are available from the first or corresponding author (Hui Zhang or Rui fen Wang) upon reasonable request.

Author contributions

H. Z. and Y. H. S. completed the sample synthesis and testing. R. F. W., S. L. A., and R. H. G. conceived the idea and accompanied the test and guidance at all stages; H. Z. and Y. H. S. wrote the manuscript; Y. W. M. was responsible for the final review; and all the authors contributed to the manuscript.

Conflicts of interest

The authors declare no competing interests.

Acknowledgements

This work was supported by Basic research business cost project in universities (0406082217), Kundulun District Science and Technology Planning Project (YF2022015), Inner Mongolia Autonomous Region Natural Science Foundation Program (2023QN05040, 2023MS02008).

References

1 J. Rockström, W. Steffen, K. Noone, *et al.*, A safe operating space for humanity, *Nature*, 2009, **461**, 472–475.
2 T. Ouyang, H. J. Wang, H. H. Huang, *et al.*, Dinuclear Metal Synergistic Catalysis Boosts Photochemical CO_2-to-CO Conversion, *Angew Chem. Int. Ed. Engl.*, 2018, **57**, 16480–16485.
3 P. Friedlingstein, M. O'Sullivan, M. W. Jones, *et al.*, Global Carbon Budget 2020, *Earth Syst. Sci. Data*, 2020, **12**, 3269–3340.
4 W. Jiang, W. Luo, R. Zong, *et al.*, Polyaniline/Carbon Nitride Nanosheets Composite Hydrogel: A Separation-Free and High-Efficient Photocatalyst with 3D Hierarchical Structure, *Small*, 2016, **12**, 4370–4378.
5 J. Zhou, Y. Li, L. Yu, *et al.*, Facile in situ fabrication of Cu_2O@Cu metal-semiconductor heterostructured nanorods for efficient visible-light driven CO_2 reduction, *Chem. Eng. J.*, 2020, **385**, 123940.
6 X. Wang, X. Chen, A. Thomas, *et al.*, Metal-Containing Carbon Nitride Compounds: A New Functional Organic–Metal Hybrid Material, *Adv. Mater.*, 2009, **21**, 1609–1612.
7 W. Liu, J. Shen, Q. Liu, *et al.*, Porous MoP network structure as co-catalyst for H_2 evolution over g-C_3N_4 nanosheets, *Appl. Surf. Sci.*, 2018, **462**, 822–830.
8 L. Tian, X. Yang, Q. Liu, *et al.*, Anchoring metal-organic framework nanoparticles on graphitic carbon nitrides for solar-driven photocatalytic hydrogen evolution, *Appl. Surf. Sci.*, 2018, **455**, 403–409.
9 Y. Sun, H. Zhang, Y. Lv, *et al.*, ZIF-8/g-C_3N_4 photocatalysts: enhancing CO_2 reduction through improved adsorption and photocatalytic performance, *RSC Adv.*, 2024, **14**, 17498–17506.
10 X. Liu, R. Ma, L. Zhuang, *et al.*, Recent developments of doped g-C_3N_4 photocatalysts for the degradation of organic pollutants, *Crit. Rev. Environ. Sci. Technol.*, 2021, **51**, 751–790.
11 Y. Li, M. Zhou, B. Cheng, *et al.*, Recent advances in g-C_3N_4-based heterojunction photocatalysts, *J. Mater. Sci. Technol.*, 2020, **56**, 1–17.
12 S. Patnaik, D. P. Sahoo and K. Parida, An overview on Ag modified g-C_3N_4 based nanostructured materials for energy and environmental applications, *Renewable Sustainable Energy Rev.*, 2018, **82**, 1297–1312.
13 J. Zhang, F. Guo and X. Wang, An Optimized and General Synthetic Strategy for Fabrication of Polymeric Carbon Nitride Nanoarchitectures, *Adv. Funct. Mater.*, 2013, **23**, 3008–3014.
14 M. H. Karimi-Harandi, M. Shabani-Nooshabadi and R. Darabi, Simultaneous determination of citalopram and selegiline using an efficient electrochemical sensor based on ZIF-8 decorated with RGO and g-C_3N_4 in real samples, *Anal. Chim. Acta*, 2022, **1203**, 339662.
15 Y. Wang, C. Zhang, Y. Zeng, *et al.*, Ag and MOFs-derived hollow Co_3O_4 decorated in the 3D g-C_3N_4 for creating dual transferring channels of electrons and holes to boost CO_2 photoreduction performance, *J. Colloid Interface Sci.*, 2022, **609**, 901–909.
16 C. C. Hou and Q. Xu, Metal–Organic Frameworks for Energy, *Adv. Energy Mater.*, 2019, **9**(23), 1801307.
17 Z. Ma, B. Guan, J. Guo, *et al.*, State of the art and prospectives of heterogeneous photocatalysts based on metal–organic frameworks (MOFs): design, modification strategies, and their applications and mechanisms in photodegradation, water splitting, and CO_2 reduction, *Catal. Sci. Technol.*, 2023, **13**, 4285–4347.
18 H. Furukawa, K. E. Cordova, M. O Keeffe, *et al.*, The Chemistry and Applications of Metal-Organic Frameworks, *Science*, 2013, **341**, 974.
19 K. Ye, Z. He, F. Wu, *et al.*, Carbon nitride-supported $CuCeO_2$ composites derived from bimetal MOF for efficiently electrocatalytic nitrogen fixation, *Int. J. Hydrogen Energy*, 2021, **46**, 35319–35329.
20 X. Zhang, X. Zhang, L. Song, *et al.*, Enhanced catalytic performance for CO oxidation and preferential CO oxidation over CuO/CeO_2 catalysts synthesized from metal

organic framework: Effects of preparation methods, *Int. J. Hydrogen Energy*, 2018, **43**, 18279–18288.

21 Y. Zhang, X. Zhang and W. Sun, In Situ Carbon-Encapsulated Copper-Doped Cerium Oxide Derived from MOFs for Boosting CO_2-to-CH_4 Electro-Conversion, *ACS Catal.*, 2023, **13**, 1545–1553.

22 S. Juntrapirom, S. Anuchai, O. Thongsook, *et al.*, Photocatalytic activity enhancement of g-C_3N_4/BiOBr in selective transformation of primary amines to imines and its reaction mechanism, *Chem. Eng. J.*, 2020, **394**, 124934.

23 L. Fan, K. Wang, K. Xu, *et al.*, Structural Isomerism of Two Ce-BTC for Fabricating Pt/CeO_2 Nanorods toward Low-Temperature CO Oxidation, *Small*, 2020, **16**, e2003597.

24 S. E. Sivan, K. H. Kang, S. J. Han, *et al.*, Facile MOF-derived one-pot synthetic approach toward Ru single atoms, nanoclusters, and nanoparticles dispersed on CeO_2 supports for enhanced ammonia synthesis, *J. Catal.*, 2022, **408**, 316–328.

25 D. O. Adekoya, M. Tahir and N. A. S. Amin, g-C_3N_4/(Cu/TiO_2) nanocomposite for enhanced photoreduction of CO_2 to CH_3OH and HCOOH under UV/visible light, *J. CO_2 Util.*, 2017, **18**, 261–274.

26 Q. Liu, C. Zeng, L. Ai, *et al.*, Boosting visible light photoreactivity of photoactive metal-organic framework: Designed plasmonic Z-scheme Ag/AgCl@MIL-53-Fe, *Appl. Catal., B*, 2018, **224**, 38–45.

27 G. Zeng, Y. Chen, L. Chen, *et al.*, Hierarchical cerium oxide derived from metal-organic frameworks for high performance supercapacitor electrodes, *Electrochim. Acta*, 2016, **222**, 773–780.

28 L. Ai, T. Tian and J. Jiang, Ultrathin Graphene Layers Encapsulating Nickel Nanoparticles Derived Metal–Organic Frameworks for Highly Efficient Electrocatalytic Hydrogen and Oxygen Evolution Reactions, *ACS Sustainable Chem. Eng.*, 2017, **5**, 4771–4777.

29 D. Pinheiro, K. R. Sunaja Devi, A. Jose, *et al.*, Box–Behnken design and experimental study of ciprofloxacin degradation over Ag_2O/CeO_2/g-C_3N_4 nanocomposites, *Int. J. Environ. Sci. Technol.*, 2021, **18**, 2303–2324.

30 S. Vignesh, S. Suganthi, B. Palanivel, *et al.*, Design a novel g-C_3N_4 based Ce_2O_3/CuO ternary photocatalysts for superior photo-degradation performance of organic mixed pollutants: Insights of Z-scheme charge transfer mechanism, *J. Phys. Chem. Solids*, 2022, **162**, 110514.

31 S. Balu, S. Velmurugan, S. Palanisamy, *et al.*, Synthesis of α-Fe_2O_3 decorated g-C_3N_4/ZnO ternary Z-scheme photocatalyst for degradation of tartrazine dye in aqueous media, *J. Taiwan Inst. Chem. Eng.*, 2019, **99**, 258–267.

32 D. J. Martin, K. Qiu, S. A. Shevlin, *et al.*, Highly Efficient Photocatalytic H_2 Evolution from Water using Visible Light and Structure-Controlled Graphitic Carbon Nitride, *Angew. Chem., Int. Ed.*, 2014, **53**, 9240–9245.

33 B. Hu, F. Cai, T. Chen, *et al.*, Hydrothermal Synthesis g-C_3N_4/Nano-$InVO_4$ Nanocomposites and Enhanced Photocatalytic Activity for Hydrogen Production under Visible Light Irradiation, *ACS Appl. Mater. Interfaces*, 2015, **7**, 18247–18256.

34 A. Kumar, S. K. Sharma, G. Sharma, *et al.*, CeO_2/g-C_3N_4/V_2O_5 ternary nano hetero-structures decorated with CQDs for enhanced photo-reduction capabilities under different light sources: Dual Z-scheme mechanism, *J. Alloys Compd.*, 2020, **838**, 155692.

35 H. N. Abdelhamid, G. A. Mahmoud and W. Sharmouk, A cerium-based MOFzyme with multi-enzyme-like activity for the disruption and inhibition of fungal recolonization, *J. Mater. Chem. B*, 2020, **8**, 7548–7556.

36 R. Yang, Z. Li, J. Zhao, *et al.*, The preparation of bimetallic cerium/copper organic framework-derived $CeCuO_x$/CNH_3-SCR catalysts, *J. Mater. Sci.*, 2024, **59**, 1298–1311.

37 H. Lu, Y. Zhou, W. Han, *et al.*, Promoting effect of ZrO_2 carrier on activity and thermal stability of CeO_2-based oxides catalysts for toluene combustion, *Appl. Catal., A*, 2013, **464–465**, 101–108.

38 L. Ai, Y. Luo, W. Huang, *et al.*, Cobalt/cerium-based metal-organic framework composites for enhanced oxygen evolution electrocatalysis, *Int. J. Hydrogen Energy*, 2022, **47**, 12893–12902.

39 Y. Tan, Z. Shu, J. Zhou, *et al.*, One-step synthesis of nanostructured g-C_3N_4/TiO_2 composite for highly enhanced visible-light photocatalytic H_2 evolution, *Appl. Catal., B*, 2018, **230**, 260–268.

40 X. Wei and H. Wang, Preparation of magnetic g-C_3N_4/Fe_3O_4/TiO_2 photocatalyst for visible light photocatalytic application, *J. Alloys Compd.*, 2018, **763**, 844–853.

41 L. Biswal, S. Nayak and K. Parida, Recent progress on strategies for the preparation of 2D/2D MXene/g-C_3N_4 nanocomposites for photocatalytic energy and environmental applications, *Catal. Sci. Technol.*, 2021, **11**, 1222–1248.

42 X. Jiao, K. Zheng, L. Liang, *et al.*, Fundamentals and challenges of ultrathin 2D photocatalysts in boosting CO_2 photoreduction, *Chem. Soc. Rev.*, 2020, **49**, 6592–6604.

43 Y. Hou, A. B. Laursen, J. Zhang, *et al.*, Layered nanojunctions for hydrogen-evolution catalysis, *Angew. Chem., Int. Ed.*, 2013, **52**, 3621–3625.

44 O. K. Varghese, M. Paulose, T. J. LaTempa, *et al.*, High-Rate Solar Photocatalytic Conversion of CO_2 and Water Vapor to Hydrocarbon Fuels, *Nano Lett.*, 2009, **9**, 731–737.

45 Y. Wang, X. Liu, X. Wang, *et al.*, Metal-organic frameworks based photocatalysts: Architecture strategies for efficient solar energy conversion, *Chem. Eng. J.*, 2021, **419**, 129459.

46 L. Zhang, K. Wong, Z. Chen, *et al.*, AgBr-Ag-Bi_2WO_6 nanojunction system: A novel and efficient photocatalyst with double visible-light active components, *Appl. Catal., A*, 2009, **363**, 221–229.

47 Z. Jiang, W. Wan, H. Li, *et al.*, A Hierarchical Z-Scheme α-Fe_2O_3/g-C_3N_4 Hybrid for Enhanced Photocatalytic CO_2 Reduction, *Adv. Mater.*, 2018, **30**(10), 1706108.

48 Y. Liu, H. Liu, H. Zhou, *et al.*, A Z-scheme mechanism of N-ZnO/g-C_3N_4 for enhanced H_2 evolution and photocatalytic degradation, *Appl. Surf. Sci.*, 2019, **466**, 133–140.